

Pattern Recognition Analysis of Age-Related Retinal Ganglion Cell Signatures in the Human Eye

Nayuta Yoshioka,^{1,2} Barbara Zangerl,^{1,2} Lisa Nivison-Smith,^{1,2} Sieu K. Khuu,² Bryan W. Jones,³ Rebecca L. Pfeiffer,³ Robert E. Marc,³ and Michael Kalloniatis^{1,2}

¹Centre for Eye Health, University of New South Wales (UNSW), Sydney, New South Wales, Australia

²School of Optometry and Vision Science, UNSW, Sydney, New South Wales, Australia

³Department of Ophthalmology, Moran Eye Center, University of Utah, Salt Lake City, Utah, United States

Correspondence: Michael Kalloniatis, Centre for Eye Health, Rupert Myers Building (South Wing), UNSW, Sydney 2052, Australia; M.Kalloniatis@unsw.edu.au.

Submitted: January 8, 2017

Accepted: May 5, 2017

Citation: Yoshioka N, Zangerl B, Nivison-Smith L, et al. Pattern recognition analysis of age-related retinal ganglion cell signatures in the human eye.

Invest Ophthalmol Vis Sci.

2017;58:3086–3099. DOI:10.1167/iov.17-21450

PURPOSE. To characterize macular ganglion cell layer (GCL) changes with age and provide a framework to assess changes in ocular disease. This study used data clustering to analyze macular GCL patterns from optical coherence tomography (OCT) in a large cohort of subjects without ocular disease.

METHODS. Single eyes of 201 patients evaluated at the Centre for Eye Health (Sydney, Australia) were retrospectively enrolled (age range, 20–85); 8 × 8 grid locations obtained from Spectralis OCT macular scans were analyzed with unsupervised classification into statistically separable classes sharing common GCL thickness and change with age. The resulting classes and gridwise data were fitted with linear and segmented linear regression curves. Additionally, normalized data were analyzed to determine regression as a percentage. Accuracy of each model was examined through comparison of predicted 50-year-old equivalent macular GCL thickness for the entire cohort to a true 50-year-old reference cohort.

RESULTS. Pattern recognition clustered GCL thickness across the macula into five to eight spatially concentric classes. *F*-test demonstrated segmented linear regression to be the most appropriate model for macular GCL change. The pattern recognition-derived and normalized model revealed less difference between the predicted macular GCL thickness and the reference cohort (average ± SD 0.19 ± 0.92 and −0.30 ± 0.61 μm) than a gridwise model (average ± SD 0.62 ± 1.43 μm).

CONCLUSIONS. Pattern recognition successfully identified statistically separable macular areas that undergo a segmented linear reduction with age. This regression model better predicted macular GCL thickness. The various unique spatial patterns revealed by pattern recognition combined with core GCL thickness data provide a framework to analyze GCL loss in ocular disease.

Keywords: ganglion cells, image analysis (clinical), pattern recognition, optical coherence tomography, aging

The retinal ganglion cell (GC) is the final output cell of the retina, receiving and modulating input from bipolar cells and amacrine cells to code for complex visual information.¹ While GCs are susceptible to a variety of disease processes,^{2–5} GC loss is also known to occur in the absence of identified disease as a part of aging.^{6–14} There is controversy regarding the spatial and temporal pattern of GC loss with age. Histologic studies have described GC loss to be linear,^{6,9,15} and a model for estimating the GC population derived from visual field sensitivity has likewise suggested a linear change.¹⁶ Studies using nerve fiber layer (NFL) thickness^{10,14,17–20} and ganglion cell layer (GCL) thickness¹² from optical coherence tomography (OCT) as a measure of GC loss have likewise suggested linear loss with age. Gao and Hollyfield,⁷ however, found that while the GC loss appeared to be linear for the macular area, loss metrics in the peripheral retina appeared logarithmic. Closer inspection of histologic data from Harman et al.⁹ and Jonas et al.⁶ suggests that there is a large variation in GC count and limited losses until after middle age. Recent studies analyzing retinal²¹ and GCL thickness¹¹ with the

OCT in the macula likewise showed greater reduction in thickness after middle age. While it is now acknowledged that peripheral retina loses GCs faster than the macula,^{7,9} knowledge of the rate of macula change is limited. Inadequate understanding of age-related GC loss may confound the detection and diagnosis of age-related pathologies involving GC loss, namely glaucoma.^{13,18,22}

OCT can provide high-density imaging and quantification of the retinal layers analogous to histologic studies,^{23–25} allowing large-scale in vivo profiling in a normal population. Thus, we sought to reinvestigate the pattern of normal age-related GC loss in the macula using OCT. Although numerous studies have quantified GC loss via NFL thickness^{10,14,17–20} and GCL thickness^{11,12} by OCT, few have analyzed these entities across temporal and spatial domains of the macula. Our study uses high-density macular cube OCT scanning to assess GC changes at 64 grid locations centered at the fovea, each grid 860 × 860 μm in size. To identify areas with similar age-related changes, we applied pattern recognition, a well-established technique for computationally clustering imaging data sets over *N* dimensions, in this case *N* =



7 age groups defined as decades. Pattern recognition visualizes complex data associations as memberships in statistically distinct theme classes²⁶ and is traditionally used for satellite remote sensing analysis.^{27–31} This analysis can be applied in other fields and has previously been used to successfully cluster retinal cells into unique signature classes according to small molecule content.^{32–36} Pattern recognition has the distinct advantage of being able to analyze large data for multiobjective optimization and at the same time assess separability of the classes using statistical tests such as transformed divergence. We hypothesized that different areas within the macula could be allocated to distinct classes according to their temporal regression signature. While a gridwise analysis enables high spatial resolution, the discriminatory power may be reduced when analyzing data that are known to have high individual variability, such as GC density.^{6,9,37} Clustering analyses allow areas with statistically proven common features to be pooled together, which can improve the discriminatory power and allow more robust analysis of highly variable data. Furthermore, classwise data may facilitate the application of these data in future research by providing a framework with which macular areas can be classed and analyzed together. We further aimed to demonstrate the application and accuracy of these models for converting GCL thickness to an age equivalent, as well as a potential tool for in vivo estimation of GC count. This improves our understanding of normal human GC population dynamics and forms the basis for future investigations involving disease, particularly if areas of retinal space can be grouped into cohesive units.

MATERIALS AND METHODS

Participants

Subjects were recruited retrospectively from patients who had been referred to the Centre for Eye Health for clinical imaging and assessments based upon risk factors or suspicion of ocular disease, but were subsequently found to have a healthy posterior pole in at least one eye. All patient records and imaging results were analyzed and reviewed by at least two experienced clinicians. Clinical data collected included visual acuity, retinal photography, Cirrus OCT scans (Macula 512 × 128 and Optic Nerve 200 × 200), intraocular pressure, and Spectralis OCT (see Macular OCT section below) scans. Participants were excluded if their intraocular pressure (IOP) was measured to be >22 mm Hg for either eye on any visit or if there was any evidence of bilateral optic nerve or retinal disease that may affect the integrity of the GCL, even if manifest unilaterally at time of examination. These included but were not limited to age-related macular degeneration, retinal dystrophies, optic neuropathies, and glaucoma as well as those identified as glaucoma suspects. Glaucoma suspects were defined in previous work,³⁸ which, in brief, included any subject with a clinical finding suspicious with regard to glaucoma on fundus appearance, imaging results, or visual fields. All eyes encompassed in this study met the following inclusion criteria: availability of a good-quality Spectralis OCT (imaging quality score > 15 dB) scan, visual acuity (VA) better than 20/25 (logMAR < 0.1) for all those under the age of 60 or better than 20/32 (logMAR < 0.2) for those older than 60, and spherical equivalent of less than ±6 diopters and astigmatism of less than 3 diopters. Unilateral ocular disease, such as central serous retinopathy, did not necessitate exclusion provided the fellow eye met the inclusion criteria. If both eyes met the inclusion criteria, one eye was randomly chosen. The scan results for the left eye were converted to right eye format. This study received ethics approval from the University of New South Wales Australia, Human Research Ethics Advisory (UNSW Australia HREA) panel.

The tenets of the Declaration of Helsinki and ethics procedures put forward by the UNSW Australia HREA were observed for subject data collection.

Macular OCT

Spectralis OCT (Heidelberg Engineering, Heidelberg, Germany) macular scans for all participants spanned 30° × 25° and consisted of 61 B-scans spaced approximately 120 μm apart. Each B-scan image was constructed from averaging at least nine frames using the acquisition software's Automatic Real Time (ART) mean function to reduce imaging noise. Scans with an overall quality score of less than 15 dB were excluded from the analysis. If multiple scans were available for the patient, the earliest scan meeting image quality criteria was selected. The measurement area was visualized on the HRA viewing module (version 6.3.4.0) consisting of an 8 × 8 grid (6880 × 6880 μm) centered on the fovea and the central horizontal line aligned over the line connecting the fovea and the middle of the optic nerve head (Figs. 1A, 1B). The GCL was automatically segmented throughout this area (Fig. 1C), and these were then manually checked and corrected for segmentation errors, defined as more than 50% difference in thickness compared to the surrounding area or any pronounced misclassification of the layers. Individual grids were excluded from the data if they contained segmentation errors that could not be corrected adequately (e.g., shadowing and distortion caused by blood vessels), or if 10% of the grid square fell outside the measurement area or was impinging on the optic nerve head.

Gridwise GCL Thickness Data Model

The cohort was separated into seven groups according to age by decade (Table 1). Normality of GCL thickness distribution for each decade group was checked with D'Agostino omnibus test (GraphPad Prism, version 6.0; GraphPad Software, La Jolla, CA, USA). The average GCL thickness was calculated for each grid location by decade (Supplementary Fig. S1). The GCL thickness data were converted to a log unit for two reasons: Linearization of the data and, as previous studies have shown, when GCL count is plotted against visual field sensitivity, another surrogate in vivo metric of GCL integrity, better correlation was achieved if GCL count was expressed as a log-unit.³⁹ Thus, the GCL thickness measurements were converted to decibel-micron units (dB, μm) using the following correlation:

$$t_{dB} = 10 \cdot \log_{10}(t_m),$$

where t_{dB} = GCL thickness in dB, μm and t_m = GCL thickness in microns.

Linear regression and segmented linear regression analysis were conducted for the GCL thickness data for each grid location using GraphPad Prism (version 6.0) to obtain a gridwise rate of GCL thickness change as a function of age.

Pattern Recognition (Clustering) Model

A grayscale heat map (Fig. 1D, first image) was generated using gridwise GCL thicknesses in microns (Supplementary Fig. S1) to provide a range of pixel values between 0 and 255. Various scaling proportions were tested, with no difference found in the final classification results. Clustering of data requires appropriate "feature selection" to be conducted, as excessive numbers of classes do not aid classification if they are not separable and lead to unnecessary burden of the model.²⁶ As a consequence, clustering is significantly affected by the applied strategy and statistical criteria. Therefore, we have adopted a clustering paradigm that has been well established in previous studies.^{27,28,30,34,35,40} Specifically, the data were analyzed with

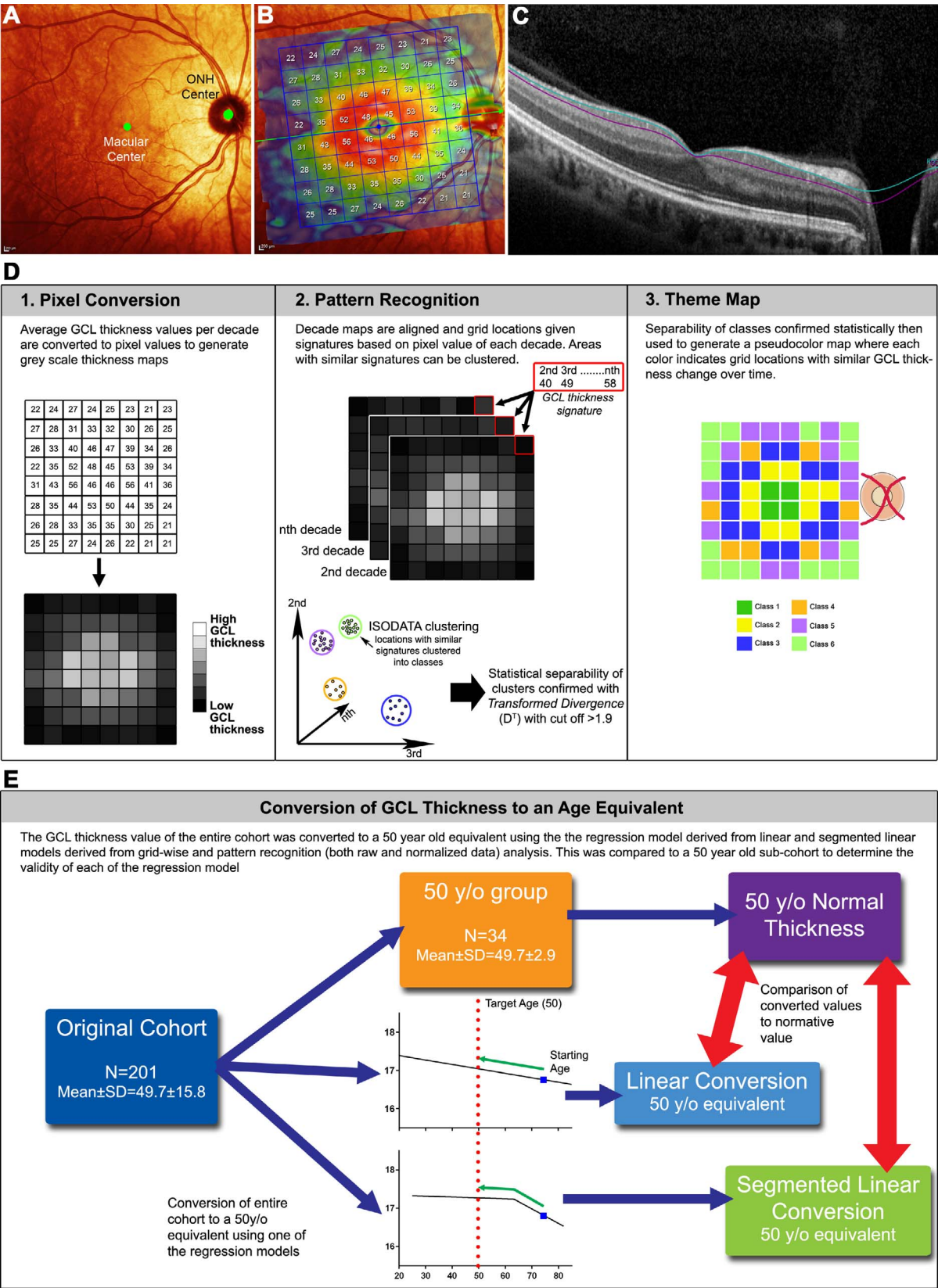


FIGURE 1. Illustration of ganglion cell analysis, conversion, and comparison. Ganglion cell layer (GCL) thickness measurements were obtained with the Spectralis OCT (A) identifying the macular and optic nerve head (ONH) center. (B) The default 64-square analysis grid of the Spectralis OCT was aligned to connect the two entities through the horizontal midline. Values for each grid location were based on average thickness values from (C) segmentation of the GCL identified between the purple and green lines. (D) Using the average GCL thickness for each decade of life, grid locations were converted into grayscale maps translating to distinct signatures. Grid locations with similar signatures were clustered in n dimensional space into classes and a color code was assigned to each class to generate a theme map indicating grid locations that has statistically similar GCL thickness

change over time. (E) The regression model derived from gridwise analysis, pattern recognition-derived classwise analysis, and normalized pattern recognition data was used to convert the entire cohort into a 50-year-old equivalent. These converted results were compared to a 50-year-old subgroup to assess the predictive value of each of these conversion models.

unsupervised classification using ISODATA clustering for each decade subgroup (PCI Geomatica, Markham, ON, Canada) (Fig. 1D, second image) generating clusters of locations within the macula with similar change in GCL thickness with age (theme classes). ISODATA clustering is a specific form of K-means clustering (a migrating means methods) and aids with feature selection by automated splitting of high variance classes and merging classes with low separability.⁴¹ Unlike traditional K-means methods, this algorithm is not bound by a predefined number of classes, but allows the class numbers to be reduced or increased appropriately within a given range. The separability of identified theme classes was statistically verified using transformed divergence (D_T).²⁶ D_T value ranges from 0 to 2, with 0 referring to inseparable clusters and 2 indicating complete separation. A value of >1.9 corresponds to a probability of correct classification of $>98\%$ ⁴² and is commonly accepted as the cutoff for statistically significant separability for clustering studies,^{27,28,30,32–35,40} as well as recommended by the manufacturer of the software.⁴³ Following classification and confirmation of separability, each distinct theme class was assigned a color for visualization in pseudocolor plot (Fig. 1D, third image). In the initial model, a single peripheral point was clustered together with the central four points corresponding with the fovea, which is inconsistent with an a priori assumption that the foveal pit is anatomically distinct from the rest of the retina.⁴⁴ Thus, in developing the final model, the central four locations corresponding to the fovea were masked and the data were reanalyzed, resulting in the reassignment of the aforementioned peripheral point with no other change in the classification. The ISODATA algorithm and statistical analysis provided the maximum number of statistically separable classes. After identifying the highest number of statistically unique theme classes using ISODATA clustering ($N = 8$ theme classes), the K-means algorithm was used to restrict the number of classes stepwise down to the lowest separable

number ($N = 5$) to further explore the effect of total number of theme classes on the provided model.

In a similar fashion to the gridwise analysis data, linear regression and segmented linear regression analysis were conducted on the eight theme classes to obtain a classwise rate of regression with age. F -test was conducted for each theme class to compare linear and segmented linear fit quality. The degree of freedom (df_1) was defined as 1 for the numerator and 12 for the denominator (df_2). The F -ratio was calculated for each theme class, defined as the quotient of the absolute sum of squares (SS_T) of the linear regression divided by the absolute SS_T of segmented linear regression. Cutoff for statistical significance was specified as >4.75 (equivalent $P < 0.05$). Paired t -tests were conducted for the absolute SS_T of the theme classes to compare the fits of the two models throughout the entire measurement area.

Furthermore, to determine if the rate of GCL change is related to the baseline thickness, the GCL thickness data for each class were analyzed after being converted to proportional data by normalizing the data to the highest value. For the purpose of statistical assessment, the proportional data were further converted to a continuous variable by an ad hoc logit transform.⁴⁵ Specifically, this was conducted by adding a small value of ε to the denominator and numerator to avoid 0 and 1 being transformed into an undefined value (i.e., $-\infty$ and $+\infty$) as outlined below:

$$\varepsilon = 1 - t'$$
$$t_{logit} = \ln \frac{t_p + \varepsilon}{1 - t_p + \varepsilon},$$

where t' = the highest non-1 proportional GCL thickness value (dB, μm) from the data set, t_p = GCL thickness (dB, μm) as a proportion, and t_{logit} = proportional data after ad hoc logit transform.

TABLE 1. Demographic Characteristics of the Study Population ($n = 201$)

Cohort	Average Age \pm SD	Range	Rx \pm SD, Diopters	IOP \pm SD, mm Hg	Sex, Percent, M:F	Laterality, Percent OD:OS	Ethnicity, Percent Euro:Asian:Oth	N
All subjects	49.7 \pm 15.8	20.2–84.9	−0.5 \pm 1.8	15.9 \pm 3.1	43:57	53:47	63:35:2	201
Cohorts by decade								
Second	25.4 \pm 2.9	20–29	−1.3 \pm 1.7	15.0 \pm 2.8	37:63	63:37	36:64:0	27
Third	34.2 \pm 3.0	30–39	−1.6 \pm 1.7	14.6 \pm 3.8	36:64	39:61	43:57:0	28
Fourth	44.9 \pm 2.8	40–49	−0.8 \pm 1.5	16.7 \pm 2.6	34:66	39:61	59:36:5	44
Fifth	55.8 \pm 2.8	50–59	−0.0 \pm 1.0	16.6 \pm 3.1	45:55	38:62	69:26:5	42
Sixth	63.5 \pm 2.9	60–69	−0.2 \pm 2.3	15.9 \pm 3.1	51:49	51:49	74:26:0	35
Seventh	73.6 \pm 2.8	70–79	+0.9 \pm 1.3	15.8 \pm 4.8	53:47	58:42	84:16:0	19
Eighth	82.0 \pm 1.6	80–85	+0.8 \pm 0.9	13.2 \pm 2.6	83:17	83:17	83:17:0	6
50 year-old equivalent cohort								
	49.7 \pm 2.9	46–55	−0.7 \pm 1.4	16.9 \pm 2.8	44:56	47:53	47:53:0	34
Curcio and Allen equivalent cohort*								
	33.5 \pm 3.3	29–39	−1.7 \pm 1.8	15.5 \pm 2.7	32:68	42:58	39:58:3	31
Curcio and Allen's cohort ³⁷								
	33.8 \pm 4.0	27–37			60:40	50:50		5

SD, standard deviation; Rx, habitual spectacle correction; OD, right eye; OS, left eye; Euro, European descent; Oth, ethnicity other than European or Asian.

* Cohort with an equivalent age distribution to Curcio and Allen's cohort³⁷ ($P = 0.845$, unpaired t -test).

Sum-of-squares *F*-test was conducted on the classwise normalized GCL thickness data to determine if all of the classes could be fitted to a single regression curve.

Agewise Conversion: Validation of Developed Regression Models

To validate the predictive value and accuracy of the regression models, GCL thicknesses for all subjects were converted to a 50-year-old equivalent using the previously developed regression models, specifically, the gridwise linear regression, classwise linear and segmented linear regression, and normalized segmented linear regression (Fig. 1E). Each resulting thickness plot was compared to the GCL thickness plots of a 50-year-old cohort ($n = 34$, Table 1) to assess for accuracy.

GC Density per Volume

GC density per GCL tissue volume (mm^3) was determined as previously described in Raza and Hood.⁴⁶ In short, GC density per mm^2 for the horizontal and vertical meridians was linearly interpolated with polar coordinates for each of the 64 grid locations using currently available histologic data of GC density per area (mm^2).³⁷ A group of age-equivalent subjects to the histologic data was selected from our cohort ($n = 31$, Table 1), and the gridwise GCL thickness was obtained from this group. GC density per mm^2 value was divided by the GCL thickness in mm to obtain the GC density in mm^3 . Furthermore, gridwise estimate of the GC count for our age-equivalent subgroup was derived by multiplying the GC density per mm^3 to the average GCL thickness and grid area ($860 \times 860 \mu\text{m}$).

RESULTS

Defining Cohort

The majority of the study subjects were of European descent (61%) with roughly a third of the cohort Asian and with a slight bias toward females (57%; Table 1). The largest deviation from these averages was observed in the eighth decade, likely due to the small sample size (Table 1). GC density per mm^2 was interpolated from previous histologic data³⁷ as described in Methods (Fig. 2A). From this, GC density per mm^3 (Fig. 2C) and the GC count (Fig. 2D) within the macular area were obtained, resulting in an estimated GC count for the total grid area of 4.68×10^5 cells, or 3.53×10^5 cells if restricted to the central 2.8-mm radius area.

Gridwise Analysis of Age-Related Changes in the GCL Thickness

GCL thickness was greatest at the paracentral macula with most areas exhibiting statistically significant rates of regression over time on linear regression analysis (Fig. 3A; mean \pm SD: -0.085 ± 0.0311 dB, μm) and reasonable coefficients of determination (mean $R^2 \pm$ SD: 0.648 ± 0.20). However, high variance was observed for both the rate of regression (range, -0.003 to -0.141 dB, μm per decade) and coefficient of determination (range R^2 : <0.01 – 0.88) throughout different regions of the measurement area. In general, the central and paracentral points showed greater rate of regression with a bias toward the nasal quadrant and areas with the lowest statistical significance, and R^2 values were primarily located peripherally, although no clear trend could be identified (Fig. 3C). Segmented linear regression analysis for the gridwise data was unsuccessful as inflection point could be identified successfully for only 23 of the 64 grid locations, while the

remaining 41 locations could not be adequately described using this model.

Pattern Recognition Analysis

Applying a cluster algorithm based on pattern recognition separated the investigated area into eight statistically distinct theme classes (implementing a $>98\%$ chance of correct classification: $D_T > 1.9$) representing macular locations with similar GCL thickness and change with age (Fig. 4A). These classes were arranged in concentric configurations, which were retained even when the number of theme classes was reduced (Fig. 5). The location provided theme maps (Figs. 4A, 5), which, when combined with the average thickness data (e.g., Supplementary Fig. S1), allowed the generation of theme class-derived data sets of GCL thickness change over time (e.g., Figs. 4B, 4C) for any theme-map combination. Theme classes plotted with the segmented linear regression exhibited negligible change in GCL thickness until the inflection point at middle to high age range (48.41–72.11 years of age; Table 2), after which greater regression rates were seen (average rate of regression before inflection: -1.79×10^{-3} dB, $\mu\text{m}/\text{decade}$, after inflection: -3.45×10^{-3} dB, $\mu\text{m}/\text{decade}$; Table 2). The average coefficient of determination for each of the regression models was found to be higher for segmented linear regression ($R^2 = 0.917$) compared to linear regression models ($R^2 = 0.663$; Table 2, Figs. 4B, 4C). This difference in coefficients of determination is to be expected, however, when comparing a simple model to a more complex one. To determine if the more complex model (segmented linear regression) is appropriate, *F*-test and paired *t*-test of the absolute SS_T was conducted. *F*-test exhibited *F*-ratios of greater than 4.75 (equivalent to $P < 0.05$) for the first four theme classes, demonstrating that segmented linear regression is a more appropriate model for these measurement areas (Table 3). The paired *t*-test did not reach statistical significance for all theme classes together ($P = 0.0543$), likely due to the high absolute SS_T exhibited by theme class 1, despite reaching significance by itself. When this class was excluded from the analysis, the relationship was found to be highly statistically significant ($P < 0.01$), thus suggesting that a segmented linear regression may be applied as a whole.

Sum-of-squares *F*-test was conducted on the normalized GCL thickness data to determine if all of the classes could be fitted to a single regression curve. Class 1 was analyzed independently on the a priori assumption that the foveal area, which it corresponds to, reflects an anatomically distinct entity. A model consisting of a different regression curve for each class was rejected by this analysis ($P = 0.983$), indicating that a single curve can adequately describe the observed regression pattern (Table 4).

Age Equivalent Conversion

To evaluate the predictive value of the aforementioned regression models, GCL thickness values of the entire cohort were converted to a 50-year-old equivalent using these models and compared to age-matched clinical data (Fig. 1E). Regression data for the linear curve were derived from both gridwise analysis (see Fig. 3) and pattern recognition analysis (Fig. 4B), while the regression data for segmented linear curve were derived from pattern recognition analysis (see Fig. 4C; Supplementary Table S1) and normalized data (Table 4), resulting in adjusted GCL thickness values (Supplementary Figs. S2B–E). The difference in GCL thickness of these converted values to the reference group (Supplementary Fig. S2A; Table 1) was found to be identical between the two linear regression models (average difference $0.67 \pm 0.638 \mu\text{m}$ for both; Supplementary Figs. S2F, S2G). When segmented linear

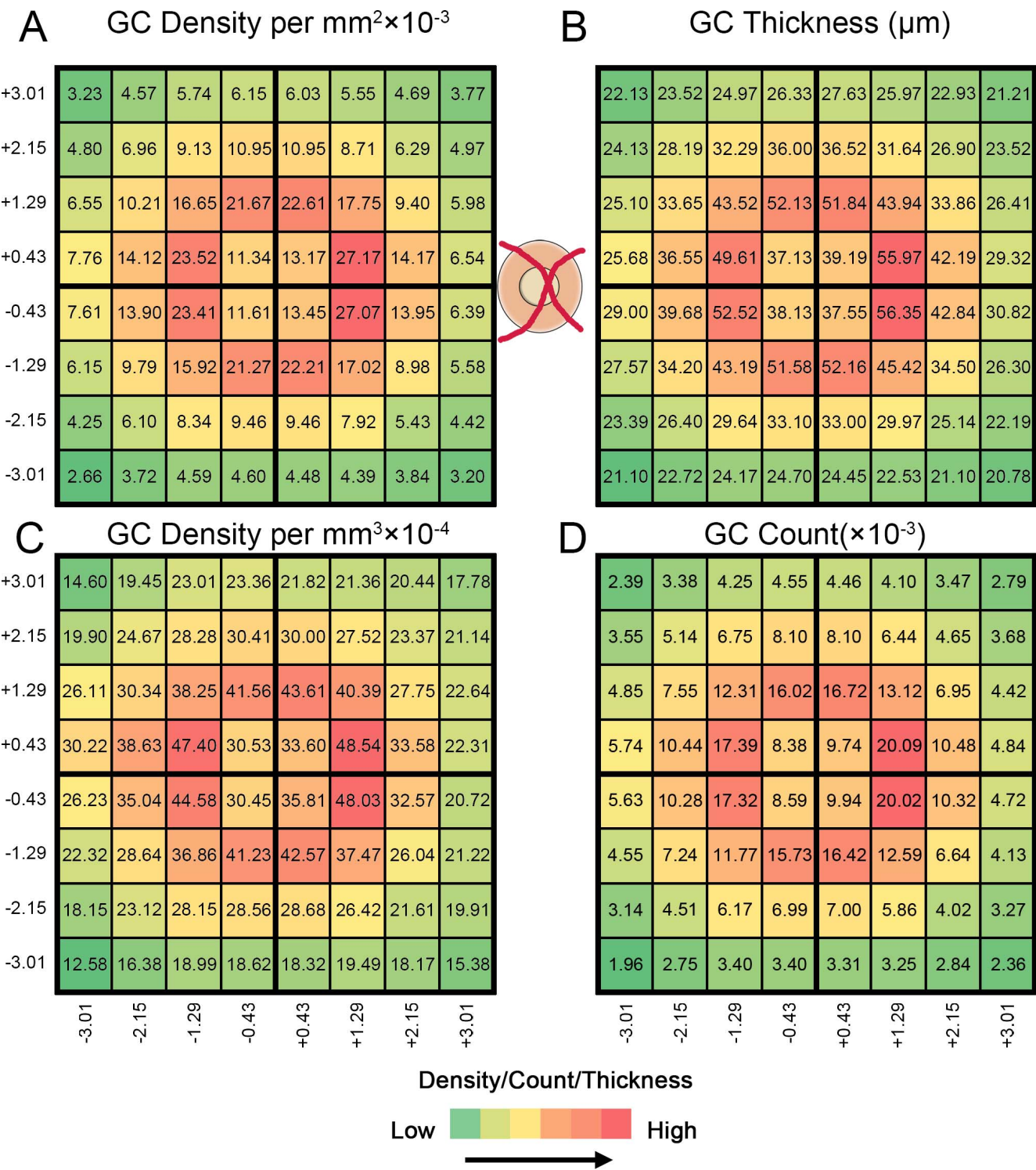


FIGURE 2. Pointwise estimation of ganglion cell density per mm^2 . Gridwise ganglion cell (GC) density per mm^2 was linearly interpolated with polar coordinates from histologic data obtained by Curcio and Allen³⁷ along the horizontal and vertical meridian (**A**). This was divided by the ganglion cell layer (GCL) thickness obtained from an age-equivalent cohort with the OCT (**B**) to obtain GC density per mm^3 for each location (**C**). This was multiplied by the grid area and the GCL thickness to obtain an estimation of GC count for each of the 64 locations (**D**).

regression was used, the disparity was reduced with both classwise and normalized analysis (0.50 ± 0.446 and $0.42 \pm 0.344 \mu\text{m}$, respectively; Supplementary Figs. S2H, S2D). Bland-Altman plots confirmed the above with the greatest bias introduced by the linear regression models (Fig. 6A; $0.51 \pm 1.11 \mu\text{m}$, Fig. 6B; $0.51 \pm 1.10 \mu\text{m}$; 95% limits of agreement)

followed by normalized regression data (Fig. 6D; $-0.30 \pm 0.61 \mu\text{m}$) and then by classwise segmented linear model (Fig. 6C; $0.19 \pm 0.92 \mu\text{m}$). While the normalized data showed larger amount of bias compared to the classwise segmented linear regression, the confidence interval was lower. When the disparity in GCL thickness between the classwise linear and

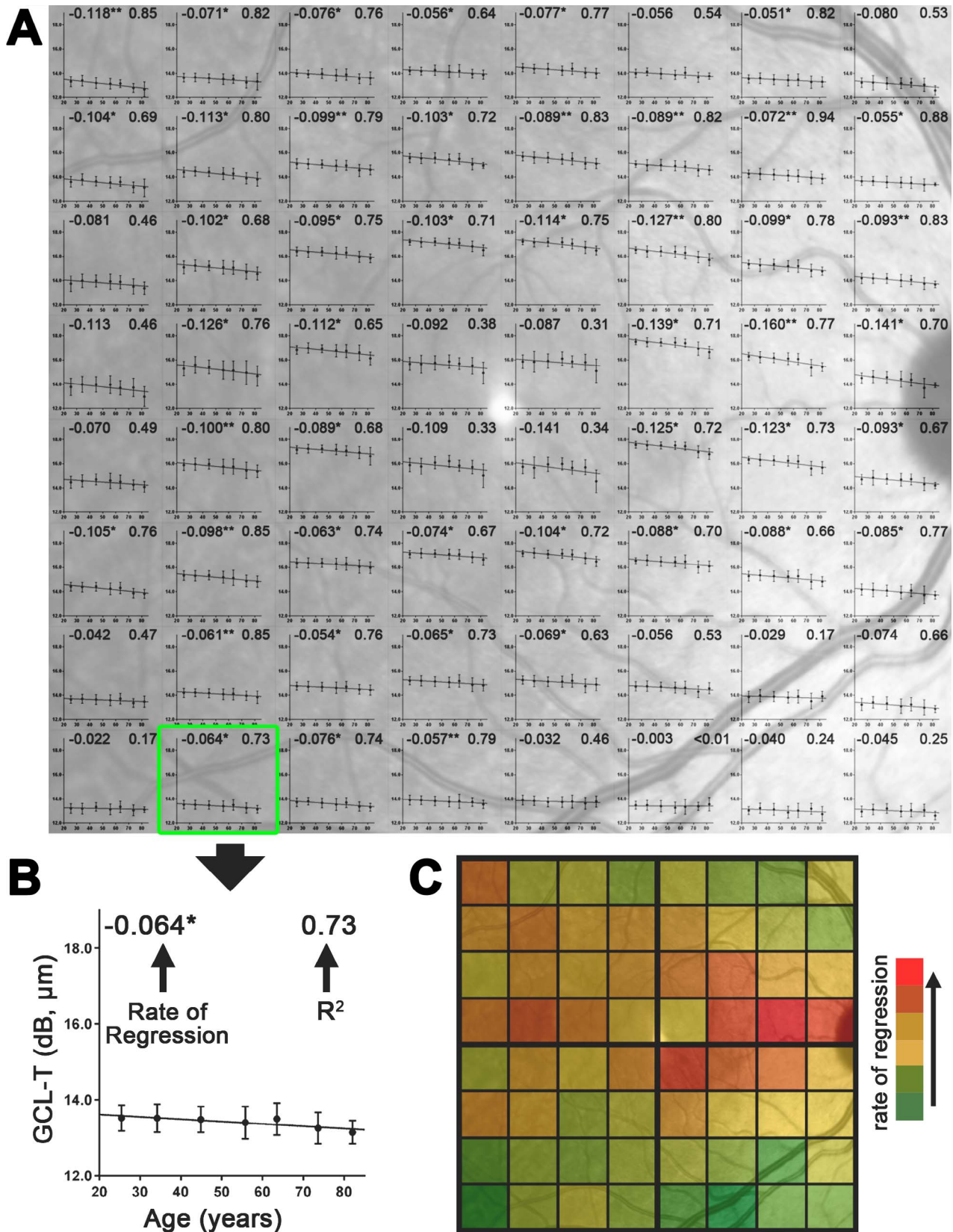


FIGURE 3. Gridwise linear regression pattern (A). Pointwise regression data of ganglion cell layer thickness plotted over age for the 64 grid locations. (B) Magnified graph indicating for each grid location the rate of regression per decade in the *top left corner* and the coefficient of determination (R^2) in the *top right* and the relevant axis scales. (C) Heat map of the rate of regression for the 64 locations where *red* indicates highest rates of regression and *green* indicates lowest rates of regression. *Error bars* show standard deviation. Statistical significance of rate of regression (nonzero) * $P < 0.05$ and ** $P < 0.01$, respectively.

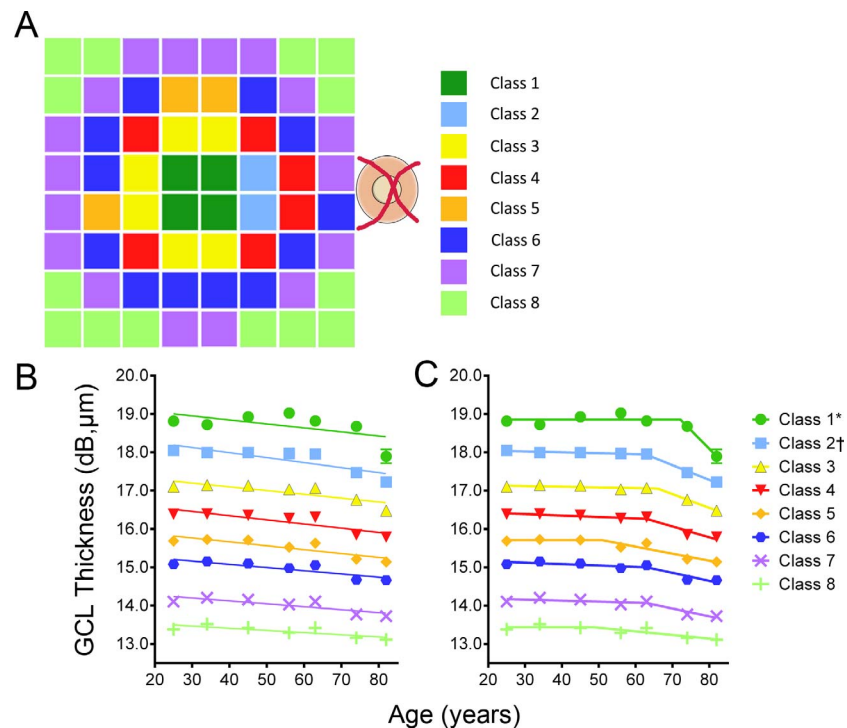


FIGURE 4. Theme class defined age-related ganglion cell layer thickness change 64 macular grid locations divided into eight theme classes as clustered using the ISODATA algorithm. The eight classes were well separated with a correct classification probability of $>98\%$ (A). Change in average ganglion cell layer thickness for each theme class over time was fitted with linear regression (B) and segmented linear regression (C). Error bars shown are standard error of mean. Asterisk and dagger indicate that these curves have been shifted by +3 and +0.5 decibel units up, respectively, for better visibility.

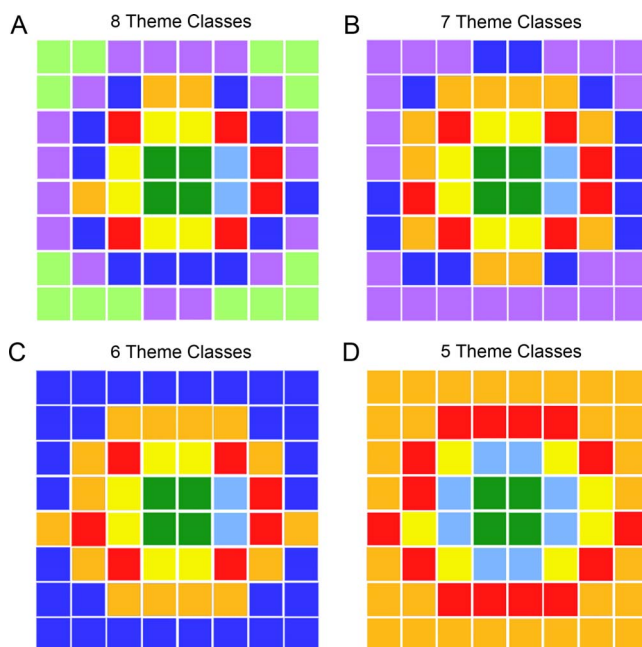


FIGURE 5. Differential configuration of theme classes. Pattern recognition analysis using ISODATA clustering and at $D_T > 1.9$ found the maximum number of statistical distinct groups (theme classes) as eight (A). The number of clusters was restricted with K-means to assess the robustness of the theme classes, allowing groups with similar characteristics to be merged together (B–D) displaying “rings” of GC locations that share similar densities and change in a similar way with age.

segmented linear models was compared directly in a Bland-Altman plot as a function of eccentricity (Fig. 6E) and theme class (Fig. 6F), the segmented linear model specifically demonstrated superior accuracy for central retinal areas (i.e., classes 1–6), while at more peripheral grids, the two models were comparable (i.e., classes 7 and 8).

DISCUSSION

OCT is able to provide information analogous to histology in vivo,^{23–25} and the advancement in image analysis enables the GCL to be assessed independently from the inner plexiform layer (IPL), which arguably allows for better assessment of GC integrity as the GCL undergoes greater absolute thinning than the IPL.^{12,47} While a number of past studies have investigated age-related retinal tissue loss with OCT,^{48–51} to the best of our knowledge this is the first investigation that not only analyzed the gridwise GCL thickness changes but also clustered them into statistically separable theme classes according to temporal regression signatures. This study demonstrated that pattern recognition can be applied to retinal thickness measurement, with the advantage of allowing a large number of data points to be analyzed for multiobjective optimization over n dimensions and, at the same time, statistically test the separability of the clusters.

Conventional gridwise analysis has the advantage of allowing analysis of an area without loss of spatial information. However, in a data set with high population variability, such as GCL thickness,^{6,9,37} the discriminatory power may be reduced. Our result demonstrated this to be the case; the spatial and temporal patterns of regression were not readily apparent with the gridwise regression data, and only a third of the measurement area could be modeled with segmented linear

TABLE 2. Ganglion Cell Layer (GCL) Thickness Regression Characteristic for the Eight Clusters Identified With Pattern Recognition Using the Linear Regression Model and Segmented Linear Regression Model. The First Segmented Linear Regression GCL Thickness Regression Rate is the Regression Rate Before Inflection, and the Second is for After Inflection (R^2 , Coefficient of Determination)

Linear Regression			
Theme Class	RGCL Thickness Regression, dB, $\mu\text{m}/\text{y}$	Intercept at Age 0	R^2
1	-1.04×10^{-2}	16.26	0.339
2	-1.24×10^{-2}	17.78	0.701
3	-9.61×10^{-3}	17.53	0.686
4	-1.09×10^{-2}	16.78	0.753
5	-1.02×10^{-2}	16.07	0.754
6	-8.41×10^{-3}	15.42	0.733
7	-7.64×10^{-3}	14.43	0.695
8	-5.73×10^{-3}	13.64	0.643
Average	-9.41×10^{-3}	15.99	0.663

Segmented Linear Regression					
Theme Class	GCL Thickness Regression, dB, $\mu\text{m}/\text{y}$	Intercept at Age 0	Age of Inflection	GCL Thickness Regression, dB, $\mu\text{m}/\text{y}$	R^2
1	0	15.86	72.11	-9.76×10^{-2}	0.933
2	-2.37×10^{-3}	17.60	62.68	-3.86×10^{-2}	0.995
3	-1.83×10^{-3}	17.18	65.88	-3.59×10^{-2}	0.987
4	-3.79×10^{-3}	16.51	62.90	-2.82×10^{-2}	0.954
5	0	15.71	50.86	-1.84×10^{-2}	0.903
6	-3.66×10^{-3}	15.23	63.00	-2.07×10^{-2}	0.902
7	-2.70×10^{-3}	14.24	63.00	-2.04×10^{-2}	0.900
8	0	13.44	48.41	-9.56×10^{-3}	0.765
Average	-1.79×10^{-3}	15.72	61.11	-3.45×10^{-3}	0.917

regression curve. Classwise analysis of pattern recognition-derived classes, on the contrary, allowed for a more powerful analysis by enabling statistically similar areas to be analyzed together and revealing that GCL regression was better modelled with a segmented linear regression than with linear regression. It has also indicated the spatial signatures to be arranged in a concentric pattern with a slight bias toward the nasal side: This is consistent with histologic data.⁸ Furthermore, these data may be able to be applied in place of gridwise regression potentially without appreciable reduction in accuracy or spatial resolution: The predicted 50-year-old equivalent GCL thicknesses with linear regression model derived from both the gridwise and classwise analysis were identical (Supplementary Figs. S2B, S2C, S2E, S2G), and the bias and confidence intervals were also similar (Figs. 6A, 6B).

TABLE 3. The Absolute Sum Square and the F -Ratio for Comparison of the Two Regression Models, Linear and Segmented Linear Regression

Theme Class	Absolute Sum Square		F -Ratio
	Linear	Segmented	
1	0.551	0.056	9.92*
2	0.171	0.003	49.71*
3	0.110	0.005	22.59*
4	0.101	0.019	5.40*
5	0.087	0.034	2.54
6	0.067	0.025	2.72
7	0.066	0.022	3.05
8	0.047	0.031	1.52

* Statistically significant difference in linear and segmented linear model (F -ratio of >4.75 , corresponding to $P < 0.05$).

Analysis of our normalized GCL thickness found the rate of GCL change expressed as a percentage to be a constant over the whole macula area (except the fovea; Table 4). In other words, regression rate was proportional to the initial GCL thickness, which also follows a concentric pattern (Supplementary Fig. S1). Therefore, it may not be surprising that when macular areas are clustered according to their pattern of regression with age, they follow a similar concentric pattern. This is consistent with a previous study that found the NFL thickness rate of change to be proportional to the initial thickness.¹⁸ To further verify the pattern of cluster found, supplementary pattern recognition analysis was conducted on selected age groups (20–29, 40–49, and 60–69) of the cohort to determine if similar classes are still present through different age groups when classified with GCL thickness alone instead of multiobjective classification. The result demonstrated similar clustering patterns to be present for all three age subgroups, with only a few points being classified differently from the original class (Supplementary Fig. S3). While a reduction in D_T

TABLE 4. Sum-of-Squares F -Test of the Segmented Linear Regression Model With Normalized GCL Thickness Rejected the Fitting of Individual Curves for Each of the Nonfoveal Classes ($P = 0.983$) and Indicated That They Can Be Fitted to a Single Curve. The First GCL Thickness Regression Rate is the Regression Rate Before Inflection and the Second Is for After Inflection (R^2 , Coefficient of Determination)

Retinal Area	GCL Thickness Regression, $\%/y$	Age of Inflection	GCL Thickness Regression, $\%/y$	R^2
Fovea (class 1)	0	72.11	-0.609	0.933
Nonfoveal classes combined	0	53.35	-0.118	0.867

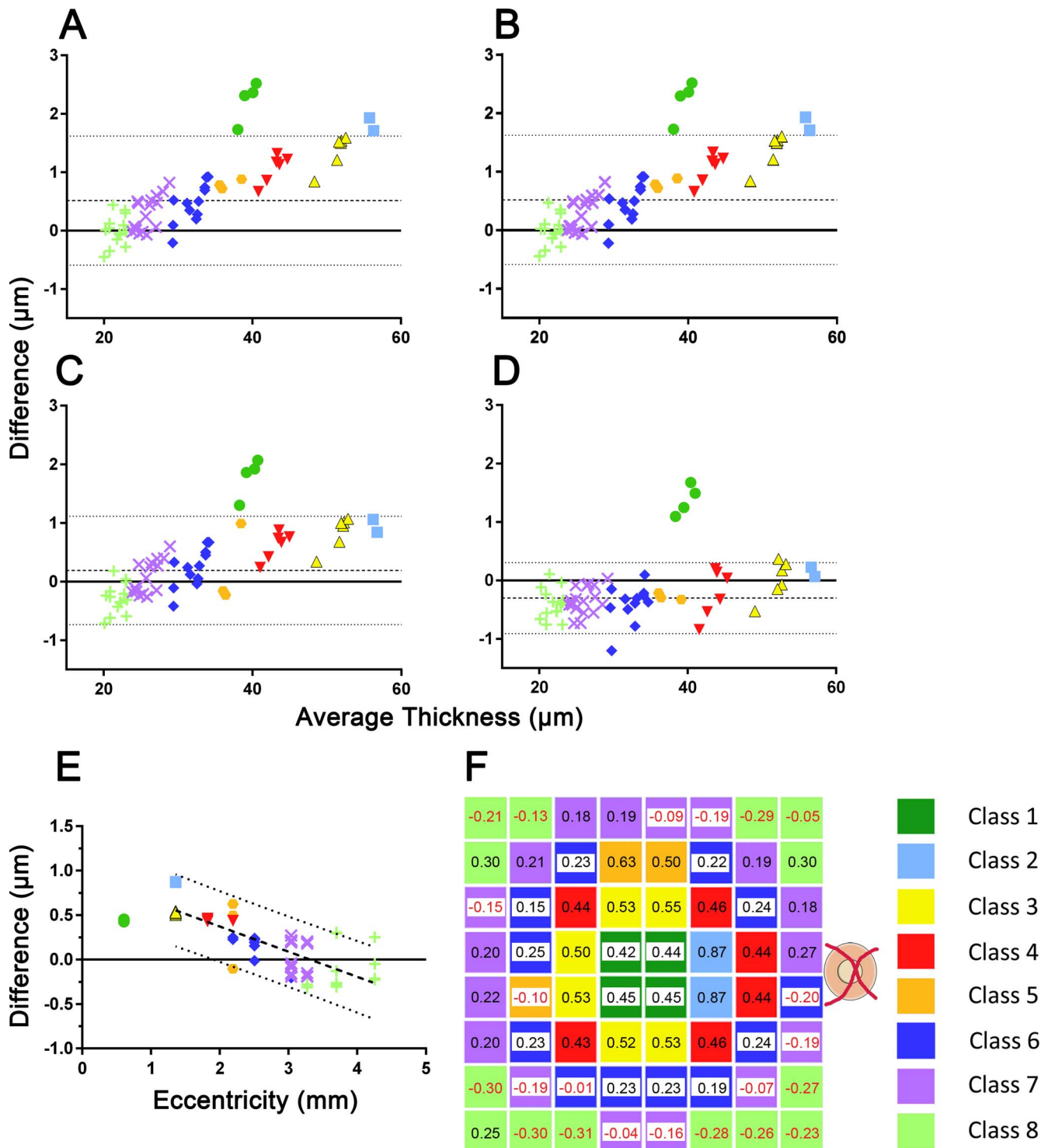


FIGURE 6. Comparison of linear and segmented linear model. Bland-Altman plot of difference ganglion cell layer (GCL) thickness between 50-year-old normative data and age-equivalent value converted with linear regression with gridwise analysis (**A**) and classwise analysis (**B**), classwise segmented linear (**C**) model, and normalized segmented linear regression (**D**) as a function of average GCL thickness. Note that class 1 areas, which constituted the foveal pits, are shown for reference but were excluded from analysis of the Bland-Altman plots as they are anatomically distinct from other retinal areas. The difference in linear (gridwise) and segmented linear (classwise) conversion values as a function of eccentricity from the fovea is shown in (**E**) and in relation to the theme classes shown in (**F**). *Red fonts* indicate areas where segmented linear model showed larger deviation from the 50-year-old equivalent value.

is expected due to the smaller sample size, it dropped below 1.9 on only one to three occasions for each subgroup, predominantly for the peripheral-most theme classes (data not shown). Furthermore, the concentric pattern persisted

when clusters with similar characteristics were merged together with the restriction of the number of theme classes using the K-means algorithm (Fig. 5). Thus, these results lend support to the concentric pattern of theme classes found on

the initial ISODATA analysis as having biological meaning. Additionally, we present a schema with varying number of concentric theme classes, which allows macular area with statistically similar GCL characteristics to be analyzed together.

The concentric nature of GCL distribution and rate of change raises the question of the suitability of a uniform gridwise measurement area for quantifying the macular area. Arguably, measurement areas need to reflect the biology of the tissue being investigated, and the difficulties of applying a uniform grid are particularly evident in the foveal grids: It does not allow one to appreciate the large thickness change gradient present in this area (Figs. 1B, 1C). Previous histologic studies for photoreceptor⁵² and GCL³⁷ count reduced the density of the sampling windows and increased window size with eccentricity, and a similar approach with OCT measurements needs to be explored.

The temporal regression pattern of macular GCL thickness was often modelled as a linear regression in previous studies,^{6,9,10,12,14–20} although there were some indications that they may follow a segmented linear regression.^{6,9,11} Comparison of the theme classes' temporal regression pattern with *F*-test suggested that segmented linear regression was a more suitable model than linear regression for the determined classes. Alternatively, the GCL thickness regression can be expressed as a normalized percentage change, in which case, the one formula can be applied to the entire macular area (except the fovea). Both of these models demonstrated accurate conversion of GCL thickness value to a given age; the classwise model demonstrated greater accuracy (less bias) while the normalized model showed greater precision (smaller confidence interval). Depending upon the intended purpose, models with greater accuracy or precision may be desired: For instance, if converting a cohort's GCL thickness data to a desired age to facilitate direct comparison to another cohort with a different age, the former may be preferable, although in cases such as repeated measurements on the same subject, the latter may be preferred. We therefore developed two alternate segmented linear regression models, each of which could be applied for different purposes. Combined with a spatial clustering schema with variable number of theme classes as shown in Figure 5, we present a framework with which future investigation of GCL can be conducted. In particular, it may be advantageous for application in structure–function studies, as it may assist in the spatial translation of data to visual field, which has different spatial distribution of data. The GCL thickness measurement was represented as a decibel scale to further facilitate future comparative study, as visual field data are also expressed in decibel scale. While a linear scale has the advantage of direct applicability to clinical scenario and a uniform scale, it was shown by previous studies that a linear relationship exists between structure and function when decibel scale was used for both variables¹⁶ and better correlation may be achieved compared to linear scale.³⁹

Gridwise GCL thickness measurement may be used as a tool for obtaining an estimate of the GC count *in vivo* for clinical and scientific purposes. While this has previously been investigated,⁴⁶ a mismatch in age between the OCT and histology cohort potentially leads to overestimation of the GC count. To address this, we conducted a similar analysis with age-matched OCT and histology data³⁷ (Table 1). The total GC count was estimated to be 3.53×10^5 cells within the central 2.8-mm radius, which was comparable to another OCT study (3.81×10^5 cells)⁴⁶ and histology (3.69×10^5 cells)³⁷-derived estimates. To further ascertain the impact of mismatch in age, the GC count was recalculated with a cohort with similar characteristics to that in Raza and Hood's⁴⁶ study (52.1 ± 9.14 years of age, $n = 135$, $P = 0.2024$, unpaired *t*-test), which did not considerably affect the estimate (3.57×10^5 cells). This is

perhaps not surprising given the nature of segmented linear regression, which showed slower regression until middle age. Disparities in GC count estimates may instead be attributed to other sources such as differences in OCT analysis methods, instrumentation, grid size, and analysis area. Additionally, the impact of nonneural elements (glia)⁵³ and displaced amacrine cells must be considered.^{37,54–56} As acknowledged in the original paper,³⁷ the histologic data utilized for this study also did not account for displaced amacrine cells and hence potentially overestimate GC density, although the impact within the macular region is expected to be low.⁵⁷ Likewise, they did not account for the presence of glial cells within the GCL.⁵³ Further investigation of displaced GC and glial cell density in the GCL of human retina may be required to refine the model further.

The temporal regression pattern for the GCL thickness was found to resemble the pattern of contrast sensitivity loss for high spatial frequency targets with age (Supplementary Fig. S4).⁵⁸ While age-related loss of contrast sensitivity is commonly acknowledged, controversy exists regarding the extent to which optical and neural changes drive the losses.^{58–65} Similarity in the temporal pattern of GC loss in our data and contrast sensitivity loss suggests that age-related neural loss could be a fundamental source of visual sensitivity loss. On the other hand, comparison to visual field sensitivity with age showed a disparity in the rate of regression; visual field sensitivity within the central 10° regressed between -0.36 and -0.77 dB per decade,⁶⁶ while the rates of GC loss were less when expressed as a linear model (approximately -0.1 dB, μm per decade, Table 2). These conflict with histology studies suggesting a direct relationship between GC count and visual field sensitivity,¹⁶ and a more recent investigation directly comparing GCL thickness measured with OCT likewise finding a direct relation between the two, albeit with a significant floor effect limiting the range where this is applicable.⁶⁷ A possible explanation is a compensatory increase in the nonneural component, leading to a reduction of neural component density per unit volume.^{10,14,22} While there are studies that show the average GC soma diameter to decrease with glaucomatous neuropathy, which may lead to reduction in neural density,^{15,68,69} it does not alter significantly with age.⁹ Furthermore, recent studies have highlighted the limitation of conventional visual field strategy utilizing stimulus size not scaled for spatial summation area,^{70–72} a potential confounding factor for any such structure–function comparison. Thus, a structure–function study comparing GC density to appropriately scaled visual stimulus and further analysis of GC density per volume may be required to clarify the relationship.

Limitations

A limitation of the study includes the decreased sample size for the higher age group, notably the 8th decade group due to the higher prevalence of ocular disease in this age group. It was found, however, that excluding the 8th decade group from the analysis had negligible impact to the pattern recognition theme classes or the regression model (data not shown).

The variability of the GCL thickness measurement with the OCT is also a potential confounding factor. It was found by a previous study that the variability of the Spectralis OCT for GCL thickness is within $3 \mu\text{m}$.⁷³ While the variability does not alter with eccentricity, this is expected to have a greater impact on the peripheral areas than the central area due to the decreased initial thickness and is likely to impact the analysis of regression pattern peripheral locations, especially if rate of regression is proportional to the baseline thickness.

Finally, since this study utilized pattern recognition to cluster retinal areas, the representation of separable classes

reflects the specific criteria chosen to define separability. As such, application of different clustering algorithms may result in changes to the statistically supported distinction of individual groups or recognize additional subgroups. However, the current clustering paradigm had been established by previous studies,^{27,28,30,34,35,40} and we have further confirmed the separability of the clusters using a validated statistical method and cutoff value ($D_T > 1.9$).^{27-35,40} Using this paradigm, we identified a maximum of eight clearly distinct classes arranged in a concentric pattern. This was consistent with the GCL thickness pattern, which was also arranged concentrically and, given that GCL regression rate is proportional to the initial thickness, the concentric arrangement of the theme classes likely reflects the biology of the GCL rather than an artefact caused by the clustering process or criteria. The robustness of these classes could be further supported if they are reproducible using different measures of separability, such as ΔK ,⁷⁴ which will be an important future step in this area once larger sample sizes are available.

CONCLUSIONS

Our study has demonstrated the advantage of pattern recognition for analyzing retinal OCT data, with the 64 grid locations rigorously grouped into a varying number of statistically separable theme classes and accentuating the temporal trend in decreasing GCL thickness. Specifically, we present two temporal regression models, one based on pattern recognition-derived theme classes and the other on normalized thickness data, and proposed a spatial clustering schema composed of a varying number of theme classes. These tools may form the basis of future investigations. For instance, either of the temporal regression models may be applied for conversion of GCL thickness data to a given age equivalent in a similar fashion to visual field regression data⁶⁶ used in previous studies.^{70,75-77} The spatial theme class schema may be implemented in structure-function concordance study by allowing multiple measurement areas to be analyzed together and facilitate spatial translation of GCL data to visual field data points. A preliminary result on similar pattern recognition study on visual field revealed a similar spatial pattern to be present when stimulus size was adjusted for spatial summation area (Kalloniatis M, et al. *IOVS* 2016;57:ARVO E-Abstract 4745), and further comparison of spatial and temporal characteristics of the two modalities may shed further light onto structure-function concordance. Finally, similar to a previous study,⁴⁶ our study presents a framework with which GC population estimates can be derived from Spectralis OCT measurement.

Acknowledgments

Supported by NHMRC 1033224; UNSW ECR Grant 2016 P535430; NY was supported through a PhD scholarship provided by Guide Dogs NSW/ACT and Australian Postgraduate Award; Guide Dogs NSW/ACT is also a partner in the NHMRC grant and provided support for LN-S; NIH NEI EY02576, EY015128, EY014800 Core Grant, an unrestricted grant from Research to Prevent Blindness to the Moran Eye Centre.

Disclosure: **N. Yoshioka**, None; **B. Zangerl**, None; **L. Nivison-Smith**, None; **S.K. Khuu**, None; **B.W. Jones**, None; **R.L. Pfeiffer**, None; **R.E. Marc**, None; **M. Kalloniatis**, None

References

- Marc RE. Functional anatomy of the neural retina. In: Albert D, Miller J, Azar D, eds. *Albert Jakobiec's Principles and Practice of Ophthalmology*. Saunders/Elsevier; 2009:443-458.
- Quigley HA, Dunkelberger GR, Green WR. Retinal ganglion cell atrophy correlated with automated perimetry in human eyes with glaucoma. *Am J Ophthalmol*. 1989;107:453-464.
- Kallenbach K, Frederiksen J. Optical coherence tomography in optic neuritis and multiple sclerosis: a review. *Eur J Neurol*. 2007;14:841-849.
- Jindahra P, Petrie A, Plant GT. Retrograde trans-synaptic retinal ganglion cell loss identified by optical coherence tomography. *Brain*. 2009;132:628-634.
- Calkins DJ, Horner PJ. The cell and molecular biology of glaucoma: axonopathy and the brain. *Invest Ophthalmol Vis Sci*. 2012;53:2482-2484.
- Jonas JB, Muller-Bergh JA, Schlotzer-Schrehardt UM, Naumann GO. Histomorphometry of the human optic nerve. *Invest Ophthalmol Vis Sci*. 1990;31:736-744.
- Gao H, Hollyfield JG. Aging of the human retina. Differential loss of neurons and retinal pigment epithelial cells. *Invest Ophthalmol Vis Sci*. 1992;33:1-17.
- Curcio CA, Drucker DN. Retinal ganglion cells in Alzheimer's disease and aging. *Ann Neurol*. 1993;33:248-257.
- Harman A, Abrahams B, Moore S, Hoskins R. Neuronal density in the human retinal ganglion cell layer from 16-77 years. *Anat Rec*. 2000;260:124-131.
- Harwerth RS, Wheat JL, Rangaswamy NV. Age-related losses of retinal ganglion cells and axons. *Invest Ophthalmol Vis Sci*. 2008;49:4437-4443.
- Mwanza JC, Durbin MK, Budenz DL, et al. Profile and predictors of normal ganglion cell-inner plexiform layer thickness measured with frequency-domain optical coherence tomography. *Invest Ophthalmol Vis Sci*. 2011;52:7872-7879.
- Demirkaya N, van Dijk HW, van Schuppen SM, et al. Effect of age on individual retinal layer thickness in normal eyes as measured with spectral-domain optical coherence tomography. *Invest Ophthalmol Vis Sci*. 2013;54:4934-4940.
- Leung CK, Ye C, Weinreb RN, Yu M, Lai G, Lam DS. Impact of age-related change of retinal nerve fiber layer and macular thicknesses on evaluation of glaucoma progression. *Ophthalmology*. 2013;120:2485-2492.
- Patel NB, Lim M, Gajjar A, Evans KB, Harwerth RS. Age-associated changes in the retinal nerve fiber layer and optic nerve head. *Invest Ophthalmol Vis Sci*. 2014;55:5134-5143.
- Kerrigan-Baumrind LA, Quigley HA, Pease ME, Kerrigan DE, Mitchell RS. Number of ganglion cells in glaucoma eyes compared with threshold visual field tests in the same persons. *Invest Ophthalmol Vis Sci*. 2000;41:741-748.
- Harwerth RS, Carter-Dawson L, Smith EL III, Barnes G, Holt WF, Crawford ML. Neural losses correlated with visual losses in clinical perimetry. *Invest Ophthalmol Vis Sci*. 2004;45:3152-3160.
- Chauhan BC, Danthurebandara VM, Sharpe GP, et al. Bruch's membrane opening minimum rim width and retinal nerve fiber layer thickness in a normal white population: a multicenter study. *Ophthalmology*. 2015;122:1786-1794.
- Vianna JR, Danthurebandara VM, Sharpe GP, et al. Importance of normal aging in estimating the rate of glaucomatous neuroretinal rim and retinal nerve fiber layer loss. *Ophthalmology*. 2015;122:2392-2398.
- Girkin CA, McGwin G Jr, Sinai MJ, et al. Variation in optic nerve and macular structure with age and race with spectral-domain optical coherence tomography. *Ophthalmology*. 2011;118:2403-2408.
- Kanamori A, Escano ME, Eno A, et al. Evaluation of the effect of aging on retinal nerve fiber layer thickness measured by optical coherence tomography. *Ophthalmologica*. 2003;217:273-278.

21. Grover S, Murthy RK, Brar VS, Chalam KV. Normative data for macular thickness by high-definition spectral-domain optical coherence tomography (spectralis). *Am J Ophthalmol*. 2009;148:266–271.
22. Harwerth RS, Wheat JL. Modeling the effects of aging on retinal ganglion cell density and nerve fiber layer thickness. *Graefes Arch Clin Exp Ophthalmol*. 2008;246:305–314.
23. Curcio CA, Messinger JD, Sloan KR, Mitra A, McGwin G, Spaide RF. Human chorioretinal layer thicknesses measured in macula-wide, high-resolution histologic sections. *Invest Ophthalmol Vis Sci*. 2011;52:3943–3954.
24. Fischer MD, Huber G, Beck SC, et al. Noninvasive, in vivo assessment of mouse retinal structure using optical coherence tomography. *PLoS One*. 2009;4:e7507.
25. Chen TC, Cense B, Miller JW, et al. Histologic correlation of in vivo optical coherence tomography images of the human retina. *Am J Ophthalmol*. 2006;141:1165–1168.
26. Richards JA. *Remote Sensing Digital Image Analysis: An Introduction*. 2nd ed. Springer-Verlag Berlin Heidelberg; 1993.
27. de Bie CAJM, Nguyen TTH, Ali A, Scarrott R, Skidmore AK. LaHMA: a landscape heterogeneity mapping method using hyper-temporal datasets. *Int J Geogr Inf Sci*. 2012;26:2177–2192.
28. Parshakov I, Coburn C, Staenz K. Automated class labeling of classified landsat TM imagery using a hyperion-generated hyperspectral library. *Photogramm Eng Remote Sensing*. 2014;80:797–805.
29. Clark PE, Seyfried MS, Harris B. Intermountain plant community classification using Landsat TM and SPOT HRV data. *J Range Manage*. 2001;54:152–160.
30. Ramachandra TV, Kumar U. Characterisation of landscape with forest fragmentation dynamics. *Journal of Geographic Information System*. 2011;3:242–253.
31. Dusseux P, Corpetti T, Hubert-Moy L, Corgne S. Combined use of multi-temporal optical and radar satellite images for grassland monitoring. *Remote Sens*. 2014;6:6163–6182.
32. Marc RE, Murry RF, Basinger SF. Pattern recognition of amino acid signatures in retinal neurons. *J Neurosci*. 1995;15:5106–5129.
33. Kalloniatis M, Marc RE, Murry RF. Amino acid signatures in the primate retina. *J Neurosci*. 1996;16:6807–6829.
34. Sun D, Vingrys AJ, Kalloniatis M. Metabolic and functional profiling of the normal rat retina. *J Comp Neurol*. 2007;505:92–113.
35. Chua J, Nivison-Smith L, Tan SS, Kalloniatis M. Metabolic profiling of the mouse retina using amino acid signatures: insight into developmental cell dispersion patterns. *Exp Neurol*. 2013;250:74–93.
36. Jones BW, Pfeiffer RL, Ferrell WD, Watt CB, Marmor M, Marc RE. Retinal remodeling in human retinitis pigmentosa. *Exp Eye Res*. 2016;150:149–165.
37. Curcio CA, Allen KA. Topography of ganglion cells in human retina. *J Comp Neurol*. 1990;300:5–25.
38. Jamous KF, Kalloniatis M, Hennessy MP, Agar A, Hayen A, Zangerl B. Clinical model assisting with the collaborative care of glaucoma patients and suspects. *Clin Exp Ophthalmol*. 2015;43:308–319.
39. Harwerth RS, Carter-Dawson L, Smith EL III, Crawford ML. Scaling the structure-function relationship for clinical perimetry. *Acta Ophthalmol Scand*. 2005;83:448–455.
40. Downie LE, Hatzopoulos KM, Pianta MJ, et al. Angiotensin type-1 receptor inhibition is neuroprotective to amacrine cells in a rat model of retinopathy of prematurity. *J Comp Neurol*. 2010;518:41–63.
41. Ball GH, Hall DJ. A clustering technique for summarizing multivariate data. *Behav Sci*. 1967;12:153–155.
42. Swain PH, King RC. Two effective feature selection criteria for multispectral remote sensing. *LARS Technical Reports*. 1973; Paper 39.
43. PCI Geomatica 2016 Online Help: SIGSEP- Signature Separability. Available at: http://www.pcigeomatics.com/geomatica-help/references/pciFunction_r/python/P_sigsep.html. Accessed February 21, 2017.
44. Scheibe P, Zocher MT, Francke M, Rauscher FG. Analysis of foveal characteristics and their asymmetries in the normal population. *Exp Eye Res*. 2016;148:1–11.
45. Warton DI, Hui FK. The arcsine is asinine: the analysis of proportions in ecology. *Ecology*. 2011;92:3–10.
46. Raza AS, Hood DC. Evaluation of the structure-function relationship in glaucoma using a novel method for estimating the number of retinal ganglion cells in the human retina. *Invest Ophthalmol Vis Sci*. 2015;56:5548–5556.
47. Moura AL, Raza AS, Lazow MA, De Moraes CG, Hood DC. Retinal ganglion cell and inner plexiform layer thickness measurements in regions of severe visual field sensitivity loss in patients with glaucoma. *Eye (Lond)*. 2012;26:1188–1193.
48. Mayama C, Saito H, Hirasawa H, et al. Diagnosis of early-stage glaucoma by grid-wise macular inner retinal layer thickness measurement and effect of compensation of disc-fovea inclination. *Invest Ophthalmol Vis Sci*. 2015;56:5681–5690.
49. Begum VU, Addepalli UK, Yadav RK, et al. Ganglion cell-inner plexiform layer thickness of high definition optical coherence tomography in perimetric and preperimetric glaucoma. *Invest Ophthalmol Vis Sci*. 2014;55:4768–4775.
50. Rao HL, Addepalli UK, Chaudhary S, et al. Ability of different scanning protocols of spectral domain optical coherence tomography to diagnose preperimetric glaucoma. *Invest Ophthalmol Vis Sci*. 2013;54:7252–7257.
51. Mwanza JC, Durbin MK, Budenz DL, et al. Glaucoma diagnostic accuracy of ganglion cell-inner plexiform layer thickness: comparison with nerve fiber layer and optic nerve head. *Ophthalmology*. 2012;119:1151–1158.
52. Curcio CA, Sloan KR, Meyers D. Computer methods for sampling, reconstruction, display and analysis of retinal whole mounts. *Vision Res*. 1989;29:529–540.
53. Ramirez JM, Trivino A, Ramirez AI, Salazar JJ, Garcia-Sanchez J. Structural specializations of human retinal glial cells. *Vision Res*. 1996;36:2029–2036.
54. Wässle H, Chun MH, Müller F. Amacrine cells in the ganglion cell layer of the cat retina. *J Comp Neurol*. 1987;265:391–408.
55. Wilder HD, Grunert U, Lee BB, Martin PR. Topography of ganglion cells and photoreceptors in the retina of a New World monkey: the marmoset *Callithrix jacchus*. *Vis Neurosci*. 1996;13:335–352.
56. Perez De Sevilla Muller L, Shelley J, Weiler R. Displaced amacrine cells of the mouse retina. *J Comp Neurol*. 2007;505:177–189.
57. Wässle H, Grunert U, Rohrenbeck J, Boycott BB. Retinal ganglion cell density and cortical magnification factor in the primate. *Vision Res*. 1990;30:1897–1911.
58. Owsley C, Sekuler R, Siemsen D. Contrast sensitivity throughout adulthood. *Vision Res*. 1983;23:689–699.
59. Owsley C. Aging and vision. *Vision Res*. 2011;51:1610–1622.
60. Guirao A, Gonzalez C, Redondo M, Geraghty E, Norrby S, Artal P. Average optical performance of the human eye as a function of age in a normal population. *Invest Ophthalmol Vis Sci*. 1999;40:203–213.
61. Artal P, Ferro M, Miranda I, Navarro R. Effects of aging in retinal image quality. *J Opt Soc Am A*. 1993;10:1656–1662.
62. Artal P, Guirao A, Berrio E, Williams DR. Compensation of corneal aberrations by the internal optics in the human eye. *J Vis*. 2001;1(1):1.

63. Elliott D, Whitaker D, MacVeigh D. Neural contribution to spatiotemporal contrast sensitivity decline in healthy ageing eyes. *Vision Res.* 1990;30:541-547.
64. Elliott DB. Contrast sensitivity decline with ageing: a neural or optical phenomenon? *Ophthalmic Physiol Opt.* 1987;7:415-419.
65. Elliott SL, Choi SS, Doble N, Hardy JL, Evans JW, Werner JS. Role of high-order aberrations in senescent changes in spatial vision. *J Vis.* 2009;9(2):24.
66. Heijl A, Lindgren G, Olsson J. Normal variability of static perimetric threshold values across the central visual field. *Arch Ophthalmol.* 1987;105:1544-1549.
67. Miraftebi A, Amini N, Morales E, et al. Macular SD-OCT outcome measures: comparison of local structure-function relationships and dynamic range. *Invest Ophthalmol Vis Sci.* 2016;57:4815-4823.
68. Quigley HA, Sanchez RM, Dunkelberger GR, L'Hernault NL, Baginski TA. Chronic glaucoma selectively damages large optic nerve fibers. *Invest Ophthalmol Vis Sci.* 1987;28:913-920.
69. Glovinsky Y, Quigley HA, Pease ME. Foveal ganglion cell loss is size dependent in experimental glaucoma. *Invest Ophthalmol Vis Sci.* 1993;34:395-400.
70. Kalloniatis M, Khuu SK. Equating spatial summation in visual field testing reveals greater loss in optic nerve disease. *Ophthalmic Physiol Opt.* 2016;36:439-452.
71. Khuu SK, Kalloniatis M. Spatial summation across the central visual field: implications for visual field testing. *J Vis.* 2015; 15(1):6.
72. Redmond T, Garway-Heath DE, Zlatkova MB, Anderson RS. Sensitivity loss in early glaucoma can be mapped to an enlargement of the area of complete spatial summation. *Invest Ophthalmol Vis Sci.* 2010;51:6540-6548.
73. Miraftebi A, Amini N, Gornbein J, et al. Local variability of macular thickness measurements with SD-OCT and influencing factors. *Trans Vis Sci Tech.* 2016;5(4):5.
74. Evanno G, Regnaut S, Goudet J. Detecting the number of clusters of individuals using the software STRUCTURE: a simulation study. *Mol Ecol.* 2005;14:2611-2620.
75. Garway-Heath DE, Caprioli J, Fitzke FW, Hitchings RA. Scaling the hill of vision: the physiological relationship between light sensitivity and ganglion cell numbers. *Invest Ophthalmol Vis Sci.* 2000;41:1774-1782.
76. Khuu SK, Kalloniatis M. Standard automated perimetry: determining spatial summation and its effect on contrast sensitivity across the visual field. *Invest Ophthalmol Vis Sci.* 2015;56:3565-3576.
77. Choi AY, Nivison-Smith L, Khuu SK, Kalloniatis M. Determining spatial summation and its effect on contrast sensitivity across the central 20 degrees of visual field. *PLoS One.* 2016; 11:e0158263.